

Effect of Texture and Mechanical Anisotropy on Flow Behaviour in Ti-6Al-4V under Superplastic Forming Conditions

L. da Silva^{a*}, G. Sivaswamy^a, L. Sun^b, S. Rahimi^a

^a Advanced Forming Research Centre, National Manufacturing Institute Scotland, University of Strathclyde, 85 Inchinnan Drive, Inchinnan, Renfrewshire PA4 9LJ, U.K

^b Hawkins & Associates, Birmingham, U.K.

*Corresponding Author, Tel: 0141 534 5523, email address: laurie.da-silva@strath.ac.uk

Abstract

The dependency of anisotropic flow behaviour on crystallographic texture is investigated in Ti-6Al-4V alloy at 750°C and 900°C and under constant strain rates of 10^{-2} , 10^{-3} and $2 \times 10^{-4} \text{ s}^{-1}$. The evolution of microstructure and crystallographic texture during these test conditions has been studied using electron backscatter diffraction (EBSD). Anisotropic flow stress behaviour was observed at 750°C irrespective of the applied strain rate. The maximum flow stress at this temperature was recorded for samples with their lengths perpendicular to the rolling direction (RD), which had $\langle 0001 \rangle // \text{Transverse Direction (TD)} \pm 20^\circ$, Basal TD texture. The presence of a banded microstructure appeared to be the prime reason for the anisotropic tensile behaviours at lower temperatures. However, at the higher temperature of 900°C isotropic deformation was achieved disregarding sample orientations, i.e., parallel and perpendicular to the RD. Rachinger grain boundary sliding along α - β boundaries, accommodated by intragranular slip, was seen to contribute towards the total strain in samples perpendicular to the RD deformed under $2 \times 10^{-4} \text{ s}^{-1}$ strain rate. As such, Rachinger grain boundary sliding is the dominant deformation mechanism in the direction perpendicular to the RD at 900°C. On the other hand, although exhibiting isotropic flow behaviour, the same texture is not observed for the samples parallel to the RD at 900°C under the same strain rate ($2 \times 10^{-4} \text{ s}^{-1}$). Thus Rachinger grain boundary sliding is not thought to be the dominating deformation mechanism for this sample orientation and potentially Lifshitz sliding is active. It is concluded that despite not having a strong effect on flow behaviour, microstructural texture determines the mechanism (i.e., Rachinger, Lifshitz) by which the superplastic deformation is driven.

Keywords

Anisotropy, Plasticity, Texture, Ti-6Al-4V, titanium, EBSD, Superplastic forming

1 Introduction

Titanium alloys are used in a variety of sectors such as aerospace, automotive and medical industries due to their sought-after properties, such as superior corrosion resistance, high strength to weight ratio and biocompatibility [1]. In particular, the dual phase α + β alloy Ti-6Al-4V (Ti-64) is frequently among chosen materials for engineering applications, due to its wide processing window that allows microstructure design and modification for good fatigue and fracture properties, high weldability and composite compatibility [2]. As a result of these unique properties, 80-90% of the titanium utilised in commercial aircrafts has the

composition of the $\alpha+\beta$ alloy Ti-64 [3]. Titanium alloys are generally considered to be difficult to form at room temperature. This is partly due to the reduced ductility caused by the limited slip systems available for the hexagonal close packed (HCP) α -phase and the extensive springback as a result of low elastic modulus [4]–[7]. These undesirable problems have been alleviated by applying hot forming and/or superplastic forming (SPF) at elevated temperatures to produce complex parts. SPF has successfully been deployed to fabricate critical structural components with complex shapes required for aerospace applications from Ti-64 [8].

Generally, materials that exhibit superplastic formability possess a fine equiaxed grain size, typically $< 20 \mu\text{m}$, and a strain rate sensitivity value, m , of > 0.36 [9]. However, SPF processes are applicable under a high temperature regime, usually at or above $0.5 T_m$, where T_m is the absolute melting temperature of the material [10, 11]. This requirement therefore is only compatible with a refined grain size where the thermal stability of the grains is ensured by preventing grain growth at the deformation temperature. This condition is satisfied when an alloy consists of either finely dispersed thermally stable particles that pin the expanding grain boundaries or when two phases are present in equal volume fractions i.e. micro-duplex materials such as Ti-64 [12]. It has been reported for example that in order to attain the best superplastic properties, the alloy system should have 40-50% volume fraction of the β -phase with body centered cubic (BCC) crystal structure [13]. Previous observations have shown that materials experience a change in texture during SPF [10], and that grain size does not change significantly after superplastic deformation implying that grains remain essentially equiaxed [14].

A definition of superplasticity was first proposed as “the ability of a polycrystalline material to exhibit, in a generally isotropic manner, very high elongations prior to failure” [15]. In uniaxial tension, elongations in excess of $\sim 200\%$ are usually indicative of superplasticity, although others [16] have suggested that this figure should be nearer 400% [12]. Industrial superplastic forming of alloys offers many advantages such as manufacturing complex shapes using one operation under low pressure [17], the ability to form high strength materials of low ductility [18], reduced tool wear and reduced cost due to the need for less tooling and fasteners [1]. However, superplastic forming also has its disadvantages such as higher costs of high strength die material, long cycle time due to the required low strain rates and higher costs of SPF materials. There are usually further costs associated with the thermomechanical treatments required to generate fine grains with an equiaxed morphology prior to superplastic forming [18]. Thus, if SPF of anisotropic sheet material with a rolling texture from previous thermomechanical processing is possible, it eliminates the need for further processing of materials prior to SPF.

Modelling of SPF processes using finite element method (FEM) is becoming increasingly of interest to researchers for obvious reasons such as tool design validation and process optimisation without the need for costly trial and error [19]. However, models have a sensitivity to the constitutive parameters employed, and the majority of current simulations are performed using isotropic criteria where in-fact something more multifarious may be

required [20]. Especially as anisotropy can influence key rheological characteristics such as the material flow behaviour and potential total elongation.

The deformation mechanism and hence the mechanical properties of Ti-64 are often seen to be influenced by the materials initial crystallographic texture. Previous studies have related the anisotropy in plastic flow at elevated temperature to different factors including (i) texture and preferred orientation of grains [21, 22], (ii) active slip systems [23, 24], (iii) banded microstructures [25]–[28] and (iv) grain size/shape/fraction [29]. Other reports suggest that all these factors co-exist such that their contributions cannot be individually distinguished [30, 31]. For example, Kaibyshev [21] investigated the existing alignment of basal crystallographic planes and observed that while superplastic deformation was occurring by grain boundary sliding (GBS) a meso-mechanism conditioned the GBS deformation termed as cooperative grain boundary sliding (CGBS) [32]. The operation of this deformation mechanism was found to be independent of the crystal lattice type and dislocations present, though interaction of lattice dislocations with grain boundaries was found to result in an acceleration of GBS and development of ‘stimulated’ GBS. The overall deformation was found to be dependent on the long-range area and structure of grain boundaries and a physical model was presented to define this behaviour.

Similarly, Packer [23] studied superplastic deformation in specimens of a eutectic Zn-Al alloy. The specimens, which were originally round samples before the test resulted in elliptical cross-sections as they superplastically deformed. This change in cross-section, along with the absence of a strong texture and the indication of a relatively small but significant proportion of randomly oriented zinc grains at the latter stages of deformation are considered as good evidences for the existence of a process accompanying slip, which restores deformed grains to a state where they are capable of further slip. Packer suggested that dynamic recrystallisation (DRX) or grain boundary migration is required to continuously regenerate the texture and achieve the morphology observed. Bowen et al. [27] studied changes in texture of both the α - and β -phases of the two-phase alloy Ti-64 to determine the mechanisms of high-temperature deformation. The alloy was extended to a strain of ~ 1.5 at 928 °C, at strain rates representative of superplastic and non-superplastic conditions. The α -phase texture showed little change with strain rate whereas the β -phase was found to be more sensitive. The β -phase texture also weakened at superplastic strain rates. Thus, it was postulated that under SPF conditions the alloy deforms predominantly by grain boundary sliding of the soft β -phase grains, with the α -phase grains remaining in their original orientations. The measured loss in texture intensity of the α -phase was attributed to the loss in texture of the secondary α -phase only.

The SPF of Ti-64 includes thermomechanical processing, phase transformation, and microstructure evolution which are still not clearly understood. The solid state phase transformation dictates the deformation mechanisms and SPF formability, and information on the effect of microstructural texture is lacking. This paper aims to present a clear understanding of the evolution of microstructure and crystallographic texture and the effect of the mechanical response during SPF of a Ti-64 alloy.

2 Experimental Procedures

2.1 High Temperature Tensile Testing

The material used in this study is a commercially produced Ti-64 alloy sheet with a 2 mm thickness. “Dog-bone” shaped tensile specimens were machined according to the ASTM standard to test the superplastic formability of materials [33] as shown in Fig. 1. The samples were manufactured with their lengths either aligned with the rolling direction (RD) or with the transverse direction (TD) of the sheet, named ORD and 90RD hereafter, respectively. Hot tensile tests were performed using a twin screw-driven Zwick/Roell (Z250) tensile testing machine with a 250 kN load cell, fitted with a 3-zones furnace filled with an argon atmosphere. The argon atmosphere was utilised to mitigate the formation of α -case on the samples during the test. The tests were conducted at 750°C and 900°C under constant strain rates of 2×10^{-4} , 10^{-3} and 10^{-2} s^{-1} . The specimens were air-cooled immediately after the tests. Flow stress curves were derived from the recorded force-displacement data with machine compliance corrected at the corresponding temperatures.

2.2 Microstructure Characterisations

Specimens for microstructural characterisations were taken from the as-received sheet, and also from material heated to the test temperatures (i.e. 750°C and 900°C) with a dwell time of 15 minutes followed by air-cooling, to explore the potential effect on the microstructure prior to the commencement of tensile testing. Microstructure characterisations were carried out on the tested tensile samples subjected to the lowest (i.e. $2 \times 10^{-4} \text{ s}^{-1}$) and highest strain rates (10^{-2} s^{-1}) at both deformation temperatures. Cross-sections parallel to both the RD and TD of the samples were utilised in the analysis of the microstructure. The metallographic samples were mounted, mechanically ground and polished to a mirror finished condition. In order to remove minor deformation layers from the surface, the mechanically polished samples were subjected to vibratory polishing using a colloidal silica suspension made of particles with a mean diameter of 0.04 μm on a Beuhler Vibrometer® 2.

Backscattered secondary electron (BSE) micrographs were recorded using a FEI Quanta 250 field emission gun scanning electron microscope (FEG-SEM) operating at 20 kV. EBSD was also used in the same FEG-SEM interfaced with an Oxford Instrument Nordlys CCD Camera. EBSD data collection was done under an accelerating voltage of 20 kV using a 100 μm diameter objective lens aperture. The acquisition time was set to 50 ms, acquiring at least 2 frames for each point. A step size of 0.3 μm was chosen to cover areas of typically 400 μm \times 300 μm for all the EBSD scans. Only the hexagonal closed packed (HCP) α -phase was selected for indexing. The average grain size was calculated automatically using EBSD software applying the equivalent circle diameter method where a minimum of 3 \times 3 pixels were required to constitute a grain. Both the acquisition and analysis of the EBSD data was achieved using HKL Channel 5 software.

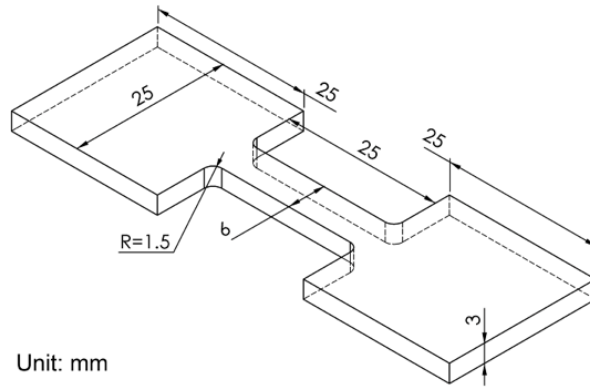


Fig 1. Schematic illustrating the geometry of the samples used for high temperature tensile testing, with the dimensions annotated (Dimensions are in mm).

3 Results

3.1 Initial Microstructure and Texture

3.1.1 *As-received Material*

The microstructure of the as-received Ti-64 alloy sheet from the ND-RD plane is given in Fig 2(a) as a BSE micrograph. The BSE micrograph shows the atomic number contrast of the microstructure, i.e. the brighter contrast representing a region containing heavier elements. As the BCC β -phase has a higher solubility of vanadium, the lighter regions are the β -phase; whilst the HCP α -phase is enriched with aluminium and therefore appears darker in the micrograph. A strongly banded microstructure was observed consisting of globularised α grains with a small fraction of β phase at grain boundaries and triple junctions. This banded microstructure can be seen more clearly in the inverse pole figure (IPF) coloured EBSD map of a selected area shown in Fig 2(b). The misorientation line profiles along the scan lines AB and CD (shown in Fig 2(d),(e)) reveal that these bands contain globularised α grains where the maximum misorientation does not exceed 15° . The average α grain size was measured to be $2.0 \pm 1.0 \mu\text{m}$. Furthermore, the IPF coloured EBSD map shows strong alignment of $\{0001\}$ poles, i.e. the c axis of the HCP α unit cell, towards TD as suggested by the presence of dominant red coloured grains within the microstructure (Fig 2(b)). The presence of a strong preferred crystallographic orientation (i.e. texture) of the α -phase in the as-received Ti-64 sheet may be more clearly depicted by the basal $\{0001\}$ and prismatic $\{10\bar{1}0\}$ pole figures presented in Fig 2(c), evaluated from the EBSD map. The $\{0001\}$ pole figure indicates a strong transverse (T) texture with the presence of a weak basal (B) component [29]. The intensity of the T texture is very high with a maximum multiple of uniform density (MUD) of 17.6. The T texture is the result of the particular thermomechanical history experienced by this Ti-64 sheet, which can be a combination of multi-directional rolling at elevated temperatures. Nevertheless, in the as-received condition, anisotropic mechanical behaviours are expected, especially at room temperature. It is well known that the elastic modulus along the TD and RD is substantially different for textured $\alpha+\beta$ titanium alloys. Furthermore, a noticeable difference exists also in the 0.2% proof strength whilst the ductility is not strongly affected by texture at room temperature.

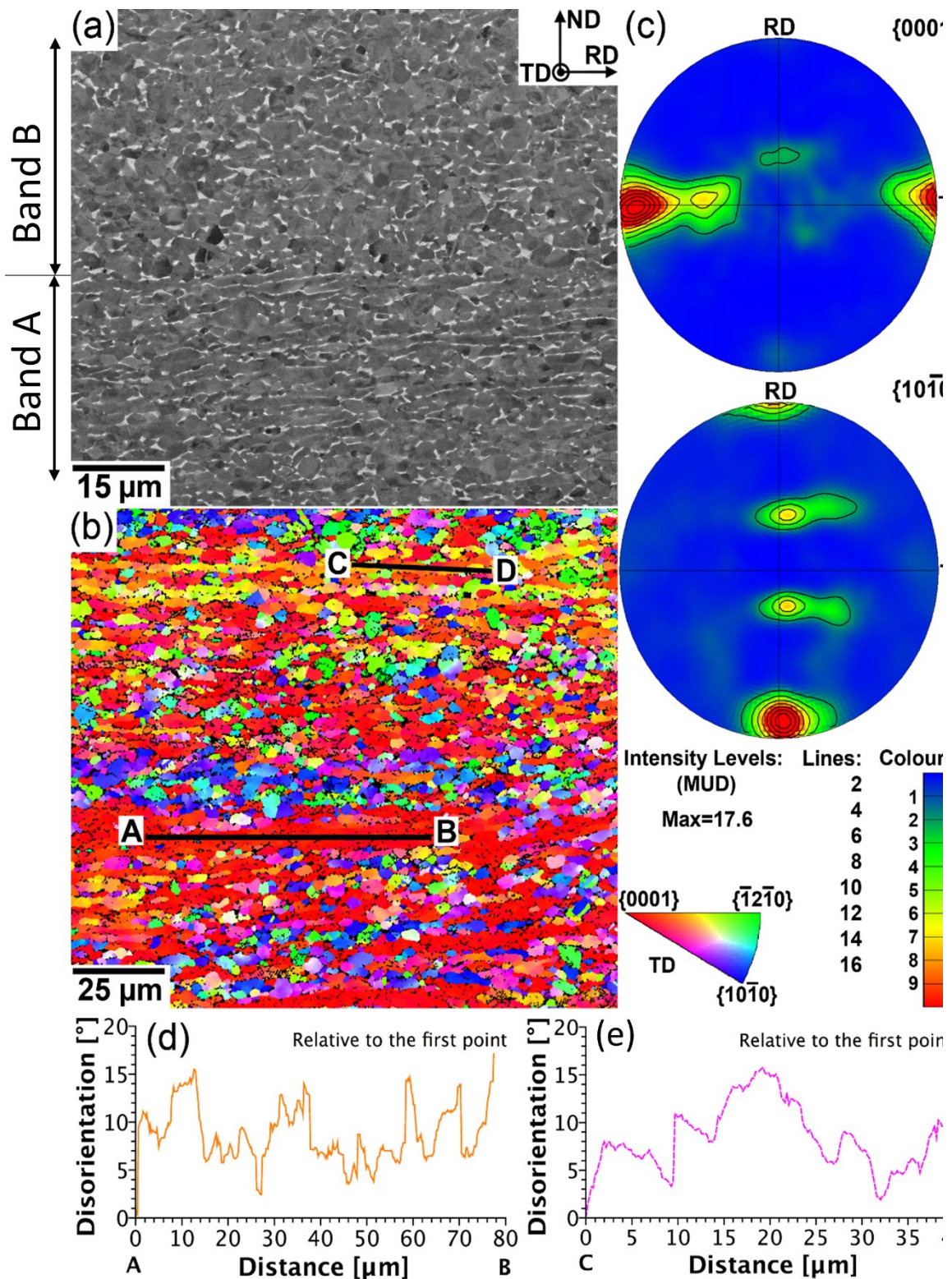


Fig 2. Microstructural characteristics of the as-received Ti-64 sheet in the as-received condition, (a) BSE micrograph showing equiaxed and elongated α grains in dark grey and β -phase as a brighter shade (b) EBSD map with IPF colouring with respect to the TD, showing the orientation of α phase, (c) $\{0001\}$ (i.e. basal) and $\{10\bar{1}0\}$ (i.e. prismatic) pole figures showing the initial texture in α phase, (d) and (e) profiles of misorientation along the AB and CD scan lines in (b) highlighting the variation in misorientation within the banded α -grains and equi-axed α grains, respectively.

3.1.2 Microstructure at test temperatures prior to tensile tests

The microstructural and texture characteristics of the Ti-64 sheet heated to the deformation temperature of 750°C, prior to the commencement of tensile tests, are given in Fig 3(a) and Fig 3(b) by a BSE micrograph and an IPF coloured EBSD map, respectively. Despite the increase in temperature, the banded microstructure still presents. As the material is heated to this temperature, the β phase field expands leading to a higher fraction of β phase in the microstructure. However, it is noted that the intensity of the transverse texture component, T, is decreased to a maximum MUD of 10.2 (Fig 3(c)) compared to that of the as-received sheet.

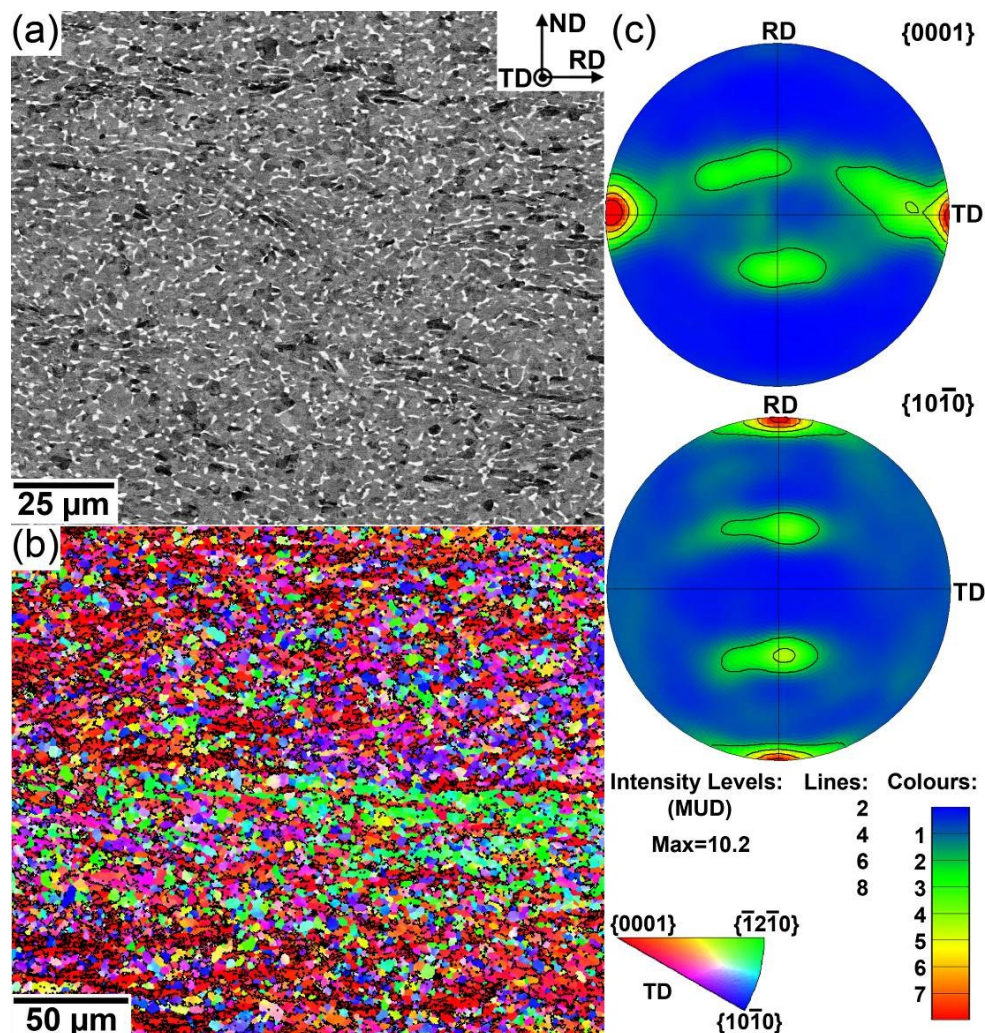


Fig 3. Microstructure characteristics of the material heated to 750 °C prior to the start of mechanical testing, (a) BSE micrograph showing the size and distribution of α and β phases, (b) IPF coloured EBSD map showing the orientation of equiaxed α grains, and (c) {0001} (i.e. basal) and {10 $\bar{1}$ 0} (i.e. prismatic) pole figures depicting a relatively strong texture of the material just before the start of mechanical testing at 750 °C.

This is likely to be due to the formation and growth of β phase at higher temperatures, at the expense of the α phase. Additionally, weakening of prismatic fiber texture components is also observed (Fig 3(c)). Fig 4 shows the microstructure and texture of the Ti-64 sheet heated to the higher temperature of 900°C prior to the commencement of tensile testing. The fraction of the β phase is observed to have increased (Fig 4(a)). The α grains appear to be more equiaxed with a calculated average grain size of $2.0 \pm 1.1 \mu\text{m}$. The intensity of the T texture component is further decreased to a maximum MUD of 8.6 whilst the intensity of the B component is further increased (MUD > 4). Nevertheless, the textures of the material just before the onset of tensile testing were still significantly strong. Therefore, anisotropic behaviours are still expected during the hot tensile tests.

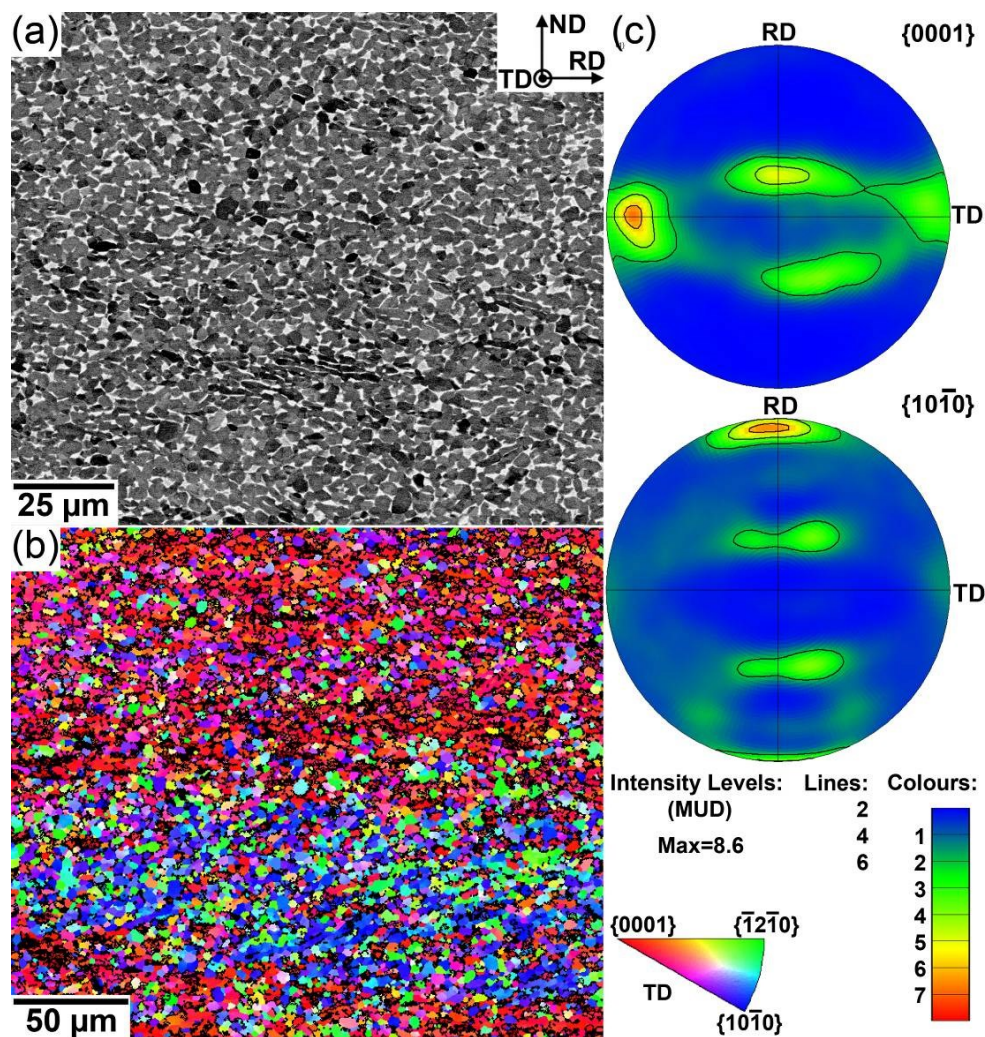


Fig 4. Microstructure characteristics of the material heated to 900 °C prior to the start of mechanical testing (a) BSE micrograph showing the size and distribution of α and β phases, (b) IPF coloured EBSD map showing the orientation of equiaxed α phase, and (c) $\{0001\}$ (i.e. basal) and $\{10\bar{1}0\}$ (i.e. prismatic) pole figures depicting a relatively strong texture of the material just before the start of mechanical testing at 900 °C.

Table 1. Summary of the measured average grain size from the EBSD maps of the as-received and at test temperatures prior to tensile test

Grain Size Analysis	As-received Condition	At 750°C Prior to test	At 900°C Prior to test
Average grain size (μm)	2.0	2.5	2.0
Standard deviation	1.0	1.2	1.1

Table 2. Summary of the measured average grain size from the EBSD data, evaluated by image processing on both cross-sections (i.e. ORD and 90RD) of the samples after tensile testing under strain rates of 0.01s^{-1} and 0.0002s^{-1} .

Temperature, T	Strain rate, $\dot{\epsilon}$ (s^{-1})	Orientation	Average grain size (μm)	Standard deviation
750°C	2×10^{-4}	ORD	2.4	1.13
		90RD	2.6	1.3
	10^{-2}	ORD	2.2	0.9
		90RD	2.1	1.0
900°C	2×10^{-4}	ORD	4.0	2.4
		90RD	2.9	1.9
	10^{-2}	ORD	1.9	0.8
		90RD	2.3	0.1

Table 1 summarises the measured average grain size as calculated from the EBSD data for the as-received material, and reference microstructures (i.e. following heating and a 15 minute dwell at test temperatures prior to mechanical testing). Similarly grain analysis results from the tested samples for strain rates of 0.01s^{-1} and 0.0002s^{-1} are given in Table 2. Data presented in Table 1 and Table 2 shows an increase in the α grain size upon heating the as-received material to the test temperatures. Measurements from different cross-sections, ORD and 90RD, appear to show different levels of α grain coarsening. For both test temperatures, higher α grain coarsening is observed after testing at the lower strain rate due to longer exposure time at the test temperature.

3.2. Flow Behaviour and Mechanical Anisotropy

It is clear from the flow curves presented in Fig 5 that testing at higher strain rates has resulted in increased peak stress, and slower strain rates has led to more elongation. A significantly higher elongation is achieved for samples subjected to the higher test temperature (900 °C) and lower strain rate (0.0002 s^{-1} , 0.001 s^{-1}) conditions, such that the furnace was not long enough to accommodate the extent of sample elongation. Therefore, for these conditions (Fig 5 (d, f)), the test was terminated long before approaching the final failure of the samples and thus maximum elongations were not reached.

For all tests carried out at 750 °C under different strain rates as well as tests carried out at 900 °C under 0.01 s^{-1} strain rate, the true stress – true strain responses approach a maximum stress (σ_{max}) shortly after 0.2% yield ($R_{p0.2}$). The measured σ_{max} appears to be consistently higher for the samples with lengths along the TD by $\approx 12\%$ and $\approx 10\%$ for the tests carried out at 750°C (Fig 5(a), Fig 5(c) and Fig 5 (e)) and 900°C (Fig 5(b)), respectively. For these

cases, once the σ_{\max} is reached an immediate slope change is observed in the stress-strain curve where the material undergoes flow softening. The magnitude and extent of flow softening can be seen to be affected by the test temperature, strain rate and sample orientation (i.e. microstructural texture). Fig 6 shows the plot of $\Theta = d\sigma/d\varepsilon_p$ as a function of plastic strain for these tests. It is apparent that at 750 °C the slope of flow softening decreases with reduced strain rate for the sample aligned with the TD exhibiting rapid softening. This has resulted in $\approx 20\%$ more elongation in the samples aligned with the RD. At 900 °C, the tests conducted on both sample orientations under 0.01 s⁻¹ strain rate (Fig 5(b) show continuous flow softening, similarly to those tested at 750°C (Fig 5(a), Fig 5(c) and Fig 5(e)), with comparable mechanical anisotropy (i.e. softening rate and % of elongation) despite a lower level of σ_{\max} . It should be noted that the non-identical response in terms of fracture strain under all strain rates at 750°C and the lower strain rate of 900°C is different for RD and TD orientations. This is thought to be primarily due to the orientation of the banded microstructure with respect to the loading direction.

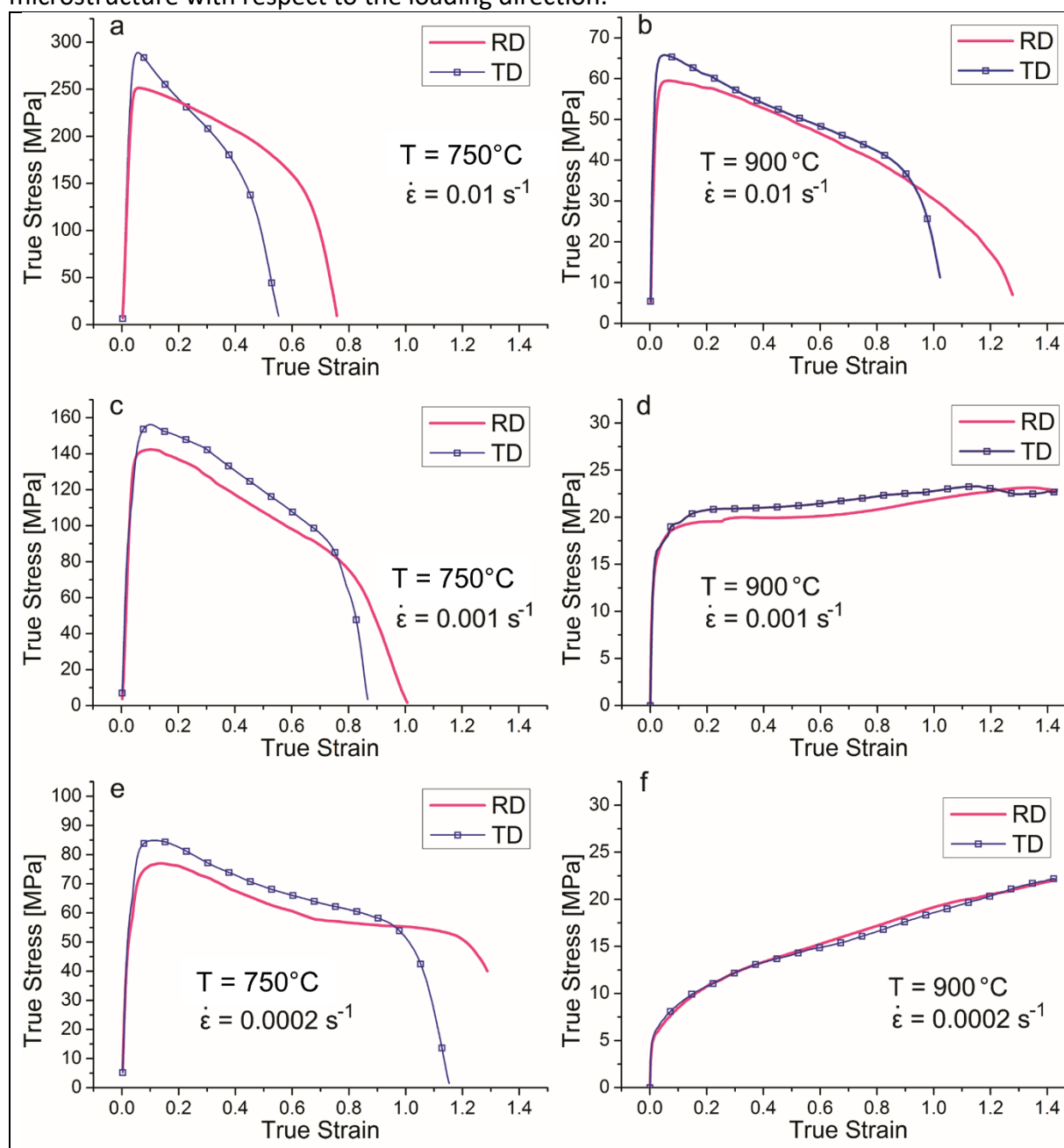


Fig 5. True stress–true strain curves of the samples loaded along the RD and TD in tension at 750 °C and 900 °C under three strain rates: , respectively, (a) and (b) $0.01s^{-1}$, (c) and (d) $0.001s^{-1}$, and (e) and (f) $0.0002s^{-1}$.

However, for slower strain rates at 900 °C (Fig 5(d) and Fig 5(f)), the results show a continuous steady-state plastic deformation under $0.001 s^{-1}$ and strain hardening under $0.0002 s^{-1}$, with negligible mechanical anisotropy (i.e. not affected by microstructural texture). There seems to be a transition from a flow softening regime through an optimum steady-state plastic deformation region to a strain hardening regime at 900 °C by decreasing the strain rate from $0.01 s^{-1}$ to $0.0002 s^{-1}$.

It can be observed that the flow stress decreases with the continuation of tensile deformation due to flow softening before the specimen eventually undergoes the necking process leading to fracture. This is the reason for the instant drop in the flow stress. The strain value at which fracture occurs, immediately after necking, is referred to as the fracture strain. It is noticed from the flow curves derived at 750°C that the values of fracture strain increases with a decrease in strain rate irrespective of the sample orientation (Fig 5(a), Fig 5(c) and Fig 5(e)). For example the value of fracture strain increases from 0.5-0.7 at the highest strain rate to 1.15-1.35 at the lowest strain rate utilised at the same test temperature of 750°C.

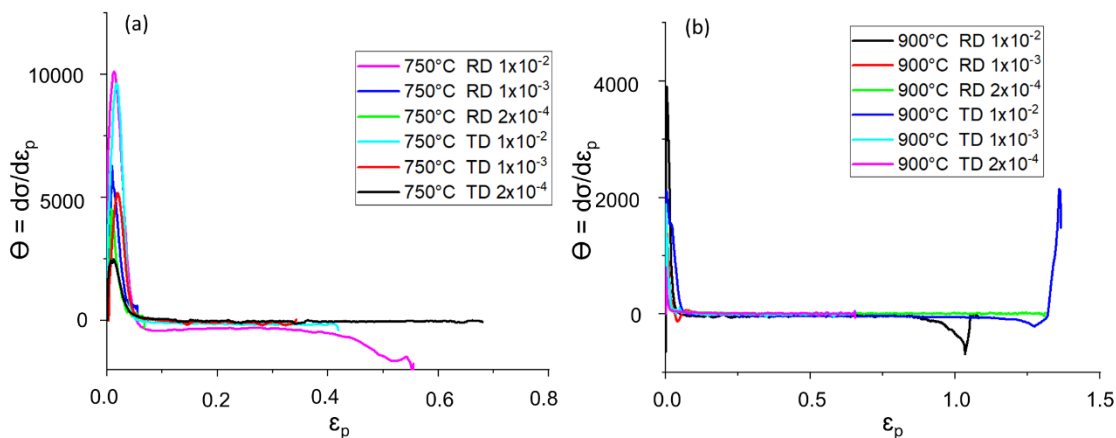


Fig 6. (a) Plots of $\Theta = d\sigma/d\varepsilon_p$ as a function of plastic strain for tensile tests at 750°C (b) Plots of $\Theta = d\sigma/d\varepsilon_p$ as a function of plastic strain for tensile tests at 900°C

Note that samples taken along the RD offered more resistance to necking as compared to samples taken perpendicular to the RD irrespective of the strain rates. Increasing the test temperature from 750°C to 900°C led to a drop in the peak flow stress values and an increase in the fracture strain values for the strain rate of $0.01s^{-1}$. A non-identical response in terms of flow behaviour is also observed for the strain rate of $0.01s^{-1}$ at 900°C between the different sample orientations, RD and TD (Fig 5(b)). A significant increase in percentage of elongation is achieved for samples subjected to the higher temperature and lower strain rate test conditions. Samples tested at 750°C at the comparatively higher strain rate of $0.001s^{-1}$ in the TD were found to have a percentage elongation of 82% as compared to samples tested at 900°C at the lower strain rate of $0.0002s^{-1}$ in the TD where 332% elongation was attained.

Strain hardening curves for samples under different test conditions are given in Fig 6. These curves demonstrate a gradual drop in strain hardening occurring immediately after the beginning of deformation under tensile load. In general, based on the strain hardening rate value (θ), the flow stress can be divided into three regions. In the initial stage of deformation ($\theta > 0$), the flow stress increases rapidly up to a critical stress, with an increase in strain. This is primarily due to the strain hardening phenomenon. During this stage, dislocation density increases due to generation and multiplication of dislocations. Once a critical threshold strain is achieved, the flow stress increases slowly up to the peak stress. During this stage, the increase in dislocation density triggers a process similar to dynamic recovery and DRX, which leads to the drop in the strain hardening rate. After the peak stress ($\theta < 0$), the flow stress decreases with strain due to the flow softening. This flow stress drop behaviour in the case of titanium alloys during hot tensile tests is primarily due to a combined effect of flow softening and ductile damage induced flow stress dropping [42]. Flow softening induced flow stress dropping is associated with dynamic recovery, dynamic globularisation of the α phase and $\alpha \rightarrow \beta$ phase transformations occurring concurrently during deformation. Additionally, ductile damage induced flow stress dropping is associated with the nucleation and growth of micro-voids and their coalescence into macro-cracks. Breaking of compatibility requirements at the interface between α and β phases and along pre-existing β grain boundaries are the main driving force for nucleation of voids during hot tensile deformation. The flow curve becomes stable ($\theta = 0$) when the dynamic softening and strain hardening reach an equilibrium. Depending on the material microstructure, strain rate and temperature, all the stages or some stages can be observed in the flow stress curve.

The stress-strain rate curves were then analysed to measure the strain rate sensitivity parameter, m , which is defined as a function stress and strain rate according to **Error! Reference source not found.**) and Equation (2) and Fig 7.

$$\sigma = C(\dot{\epsilon})^m \quad (1)$$

$$\log \sigma = m \log \dot{\epsilon} + \log C \quad (2)$$

The plots shown in Fig 7 the superplastic formability of the material at higher temperatures as the calculated m values significantly increase from ~ 0.35 to ~ 0.6 for the tests conducted at 900°C compared to 750°C . Though the m value for different sample orientations at a given temperature looks very similar.

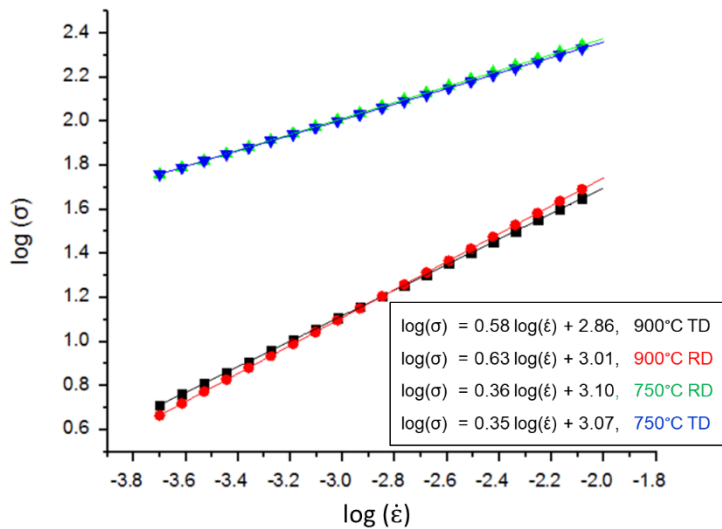


Fig 7. Plots of $\log(\sigma)$ vs. $\log(\dot{\epsilon})$ used for the calculation of strain rate sensitivity (m) at each test temperature.

3.3. Evolution of microstructure and crystallographic texture

The microstructure and crystallographic texture of samples tested under the fastest and slowest strain rates at both temperatures were investigated to understand the dominant deformation mechanisms operating during the tests. Fig 8 and Fig 9 show the microstructures of samples with their lengths aligned with the RD and TD, respectively. BSE micrographs and IPF maps from the EBSD scans of the samples are provided for the maximum and minimum strain rate condition at both 750 °C and 900 °C.

It can be seen in Fig 8(a) and (e) as well as in Fig 9(a) and Fig 9(e) that for the tests carried out at 750 °C, at the faster strain rate of 0.01 s^{-1} , nothing significant has occurred during the test along both sample orientations. The fraction of primary α grains is almost the same as those of the as-received condition (Fig 2) and of the microstructure prior to the test (Fig 3). In both orientations at the slower strain rate of 0.002 s^{-1} , there appears to be an increase in grain size by $\approx 0.35 \mu\text{m}$ due to increased time at the test temperature of 750 °C. This is clearly seen from BSE micrographs given in Fig 8(i) and Fig 8(m).

At the higher temperature of 900 °C, a significant $\alpha \rightarrow \beta$ transformation appears to occur during the test that is visible for all strain rates shown (Fig 8(c), Fig 8(g), Fig 8(k) and Fig 8(o)). Additionally, it is also apparent that an increase in the temperature has resulted in growth of primary α grains and an increase in grain size, by $\approx 1 \mu\text{m}$ in the case of the slowest strain rate. IPF maps given in Fig 8 and Fig 9 also shows that both sample orientations retain the initial texture, a preferential alignment of basal planes $\{0001\}$ with the TD, under 0.01 s^{-1} strain rate at both temperatures, though the texture is weakened. At 900°C in the ND-TD plane (Fig 8(d)), a macro band is visible in the centre of the EBSD IPF map, despite the higher test temperature. The EBSD IPF maps also show clusters of fine grain networks developed during the tests, which is more apparent in the tests carried out at 750 °C (see Fig 8 (a),(b),(e), (f) and Fig 9 (a), (b), (e), (f)), that are likely to be due to DRX. DRX is expected to occur at the higher test temperature of 900°C, however due to quick and significant grain growth this is less apparent. Fig 10 and Fig 11 show the basal $\{0001\}$ and prismatic $\{10-10\}$ pole figures for the samples tested along the RD and TD, respectively. Note that only the results from samples

subjected to higher and lower strain rates are presented for each test temperature. For the samples tested along the RD at 750 °C under 0.01 s⁻¹ strain rate (Fig 10(a) and Fig (b)) the initial basal and prismatic textures are retained with slightly lower intensities compared to those of the as-received material. However, testing along the RD at the same temperature, but under the slower strain rate of 0.0002 s⁻¹, has resulted in the dissipation of both the basal and prismatic textures (Fig 10(c) and Fig 10(d)). For the samples tested along the RD at 900 °C, whilst the basal texture remains under both strain rates, similarly to the results of experiments at 750 °C the prismatic texture disappears. Conversely, for the samples tested along the TD for all conditions (Fig 11), the randomness of the crystal orientation increases and as a result both basal and prismatic textures weaken with the accumulation of superplastic strains. Interestingly, the texture behaviour of samples tested at 900°C at the lower strain rate of 0.0002 s⁻¹ along the TD differs from the results of the same test conditions on the sample aligned with the RD despite both showing superplastic flow behaviour in exactly the same manner (Fig 5).

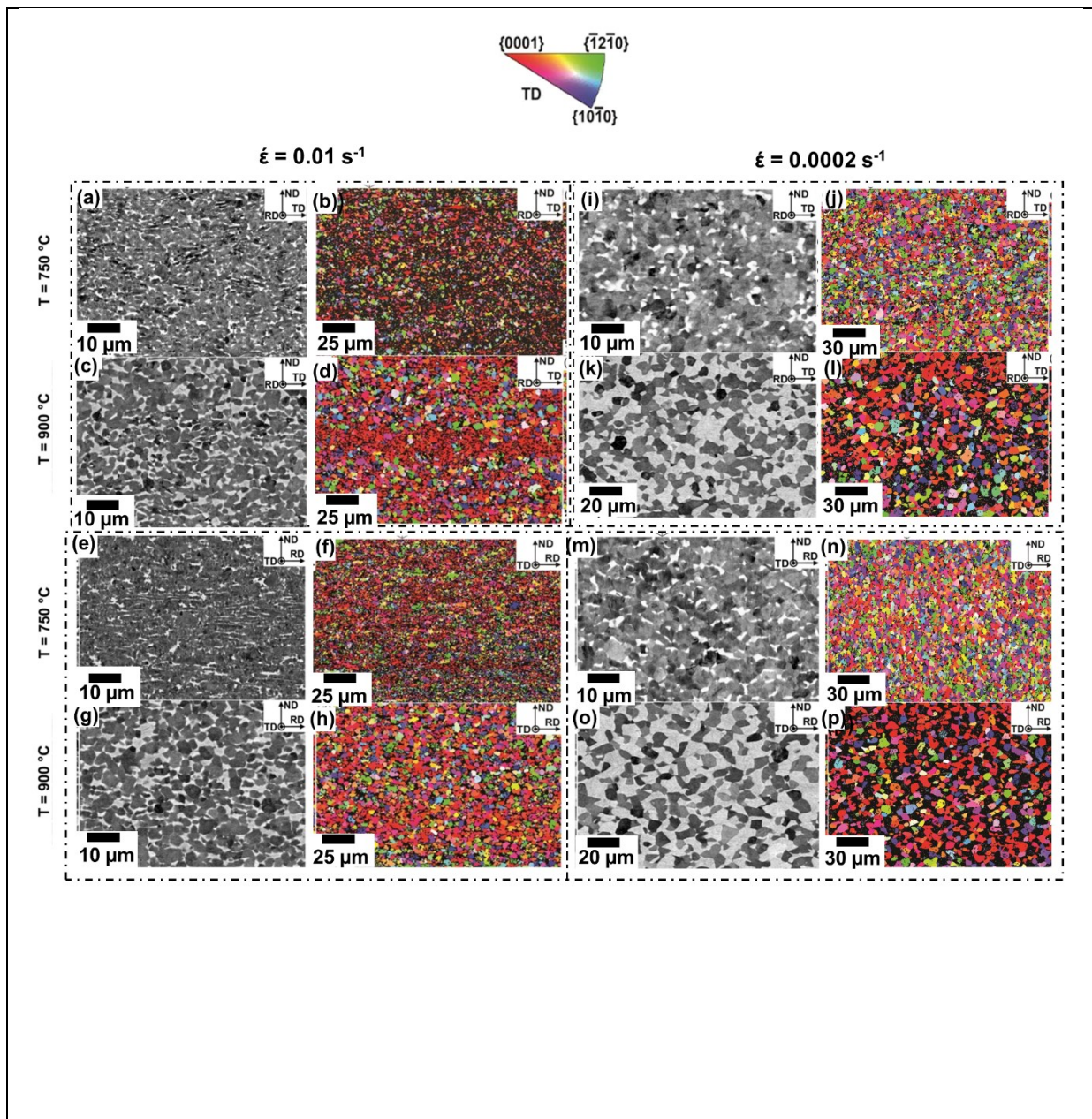


Fig 8. BSE micrographs and EBSD IPF maps of the samples tested along the RD under a strain rate of 0.01 s^{-1} at 750°C and 900°C taken from the ND-TD plane (a-d) and from the ND-RD plane (e-h). Under a strain rate of 0.0002 s^{-1} at 750°C and 900°C taken from the ND-TD plane (i-l) and from the ND-RD plane (m-p). Schematic illustrating the planes used for recording the micrographs from the tested sample is also provided as insert.

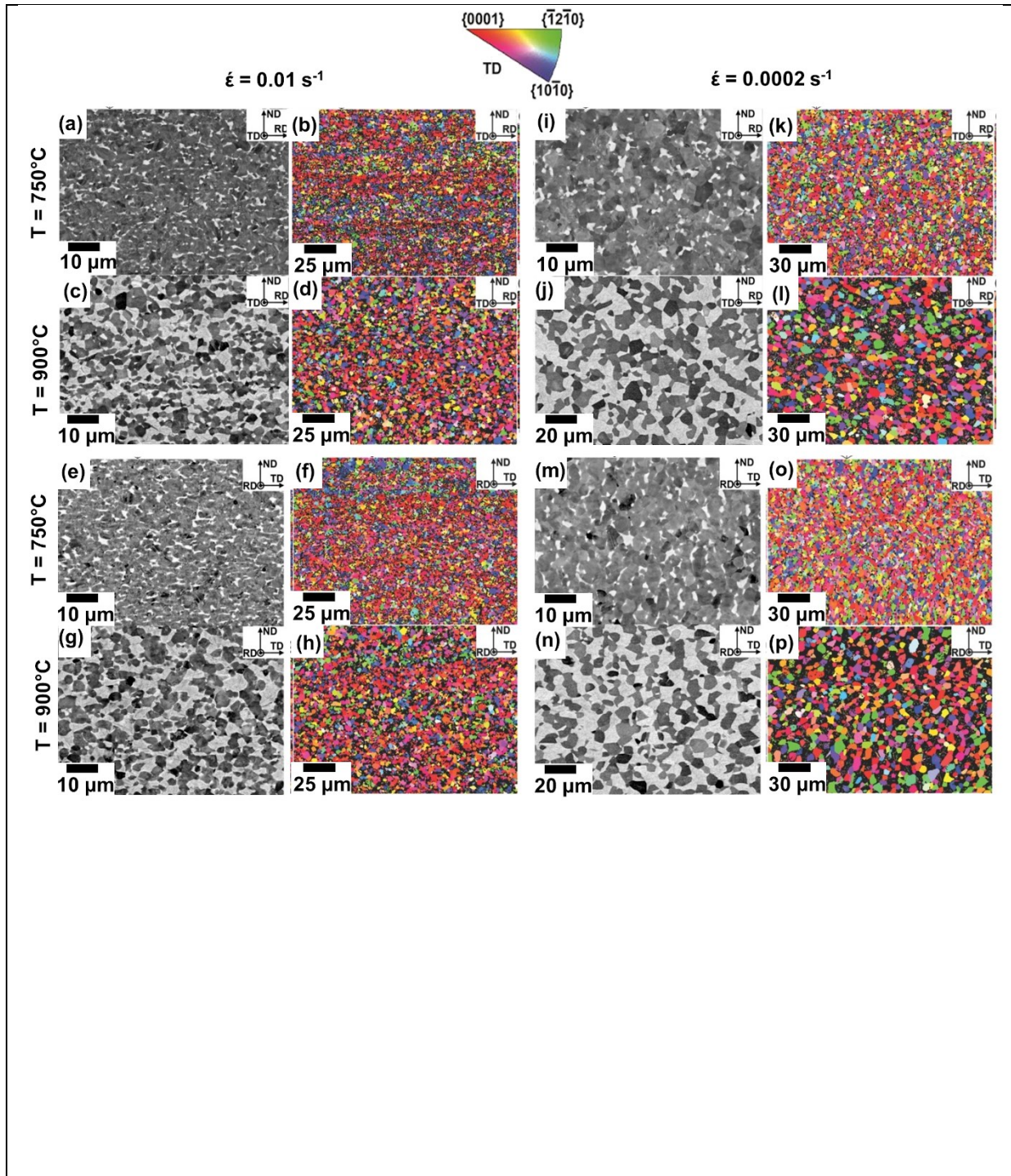


Fig 9. BSE micrographs and EBSD IPF maps of the samples tested along the TD under a strain rate of 0.01 s^{-1} at $750 \text{ }^\circ\text{C}$ and 900°C taken from the ND-RD plane (a-d) and from the ND-TD plane (e-h). Under a strain rate of 0.0002s^{-1} at $750 \text{ }^\circ\text{C}$ and 900°C taken from the ND-RD plane (i-l) and from the ND-TD plane (m-p).

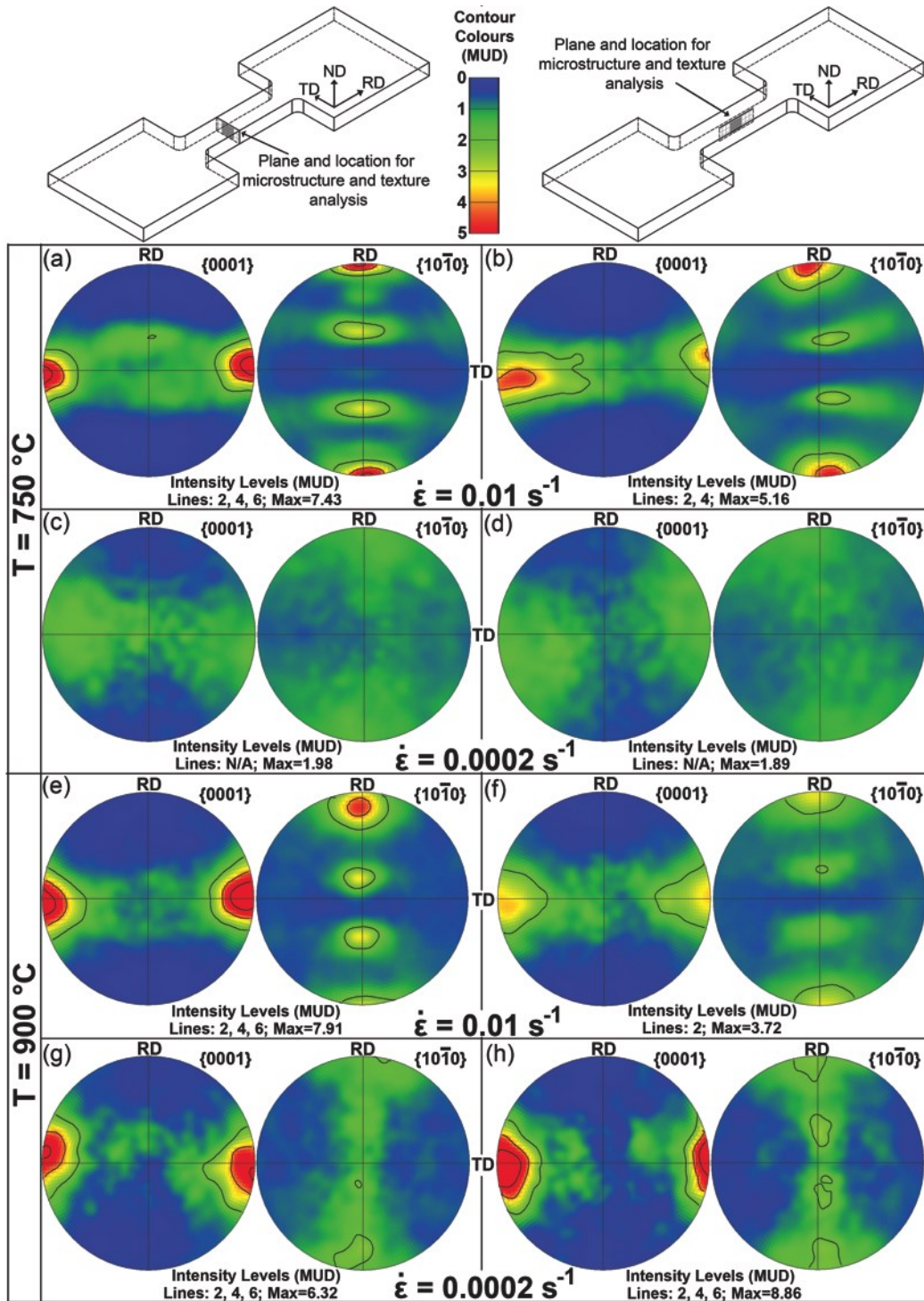


Fig 10. Basal (0001) and prismatic (10-10) polefigures plotted from the EBSD maps of α phase of the samples tested along the RD at (a) $750 \text{ }^\circ\text{C}$ and under 0.01 s^{-1} , (b) $750 \text{ }^\circ\text{C}$ and under 0.0002 s^{-1} , (c) $900 \text{ }^\circ\text{C}$ and under 0.01 s^{-1} , and (d) $900 \text{ }^\circ\text{C}$ and under 0.0002 s^{-1} .

under 0.0002 s^{-1} , (c) $900 \text{ }^{\circ}\text{C}$ and under 0.01 s^{-1} , and (d) $900 \text{ }^{\circ}\text{C}$ and under 0.0002 s^{-1} . Schematic illustrating the planes used for analysis from the tested sample is also provided as an insert.

4 Discussion

It was shown in Fig 5 that the measured σ_{\max} for the samples tested along the TD at 750°C was higher than the samples tested along the RD while their elongation behaviour was the opposite, disregarding the magnitude of the applied strain rate. A similar trend was also observed for the test carried out at $900 \text{ }^{\circ}\text{C}$ under the highest applied strain rate (0.01 s^{-1}), although this wasn't the case for the intermediate (i.e. 0.001 s^{-1}) and slowest (i.e. 0.0002 s^{-1}) strain rates. This implies that the material undergoes different deformation mechanisms depending on the test temperature and the applied strain rate. Accordingly, a basic deformation plot can be constructed for this material (Fig 12(a)) based on the applied temperature and strain rate, in which different regimes can be identified, similarly to the approach presented in a study reported earlier [34]. For the tests conducted in this study, the applied conditions led to three regimes where different deformation mechanisms are dominant within each. These are, (1) a low temperature and relatively high strain rate regime with low strain rate sensitivity (Fig 7) where flow softening was observed in the stress-strain curves (Fig 5(a), Fig 5(c), and Fig 5(e)), during which plastic strain is compensated for via DRV, DRX and cavitation damage; (2) a high temperature and intermediate strain rate regime with high strain rate sensitivity (Fig 7) and a steady-state stress strain curve (Fig 5) during which GBS occurs with stable grain size and absence of cavitation; and (3) a high temperature and very slow strain rate regime with very high strain rate sensitivity under which plastic strain is accommodated by diffusion creep and grain growth. These are shown schematically in Fig 12(b).

The low ductility observed for all tests at $750 \text{ }^{\circ}\text{C}$ and also under the 0.01 s^{-1} strain rate at $900 \text{ }^{\circ}\text{C}$ has previously been shown to be due to the formation of cavitation and their growth beyond a threshold value that leads to a premature failure [34]. Post-test observations of voids formed under different conditions (Fig 13) confirms previous findings in [34], as the size and volume fraction of the cavities for the lower temperature and higher strain rates (Fig 13(a) and Fig 13(b)) were found to be significantly larger than those of the tests exhibited steady state superplastic forming (Fig 13(c) and Fig 13(d)). Ductile damage induced flow softening is therefore associated with the nucleation and growth of micro-voids and their coalescence into macro-cracks. Breakage of the compatibility requirement between different grain boundaries (i.e., α - β , α - α , β - β) is the main driving force for nucleation of voids during hot tensile deformation. A previous report showed that interactions between hard α - α boundaries facilitate the nucleation of voids and cavities more than those of α - β and β - β boundaries [34]. Therefore, the materials subjected to the lower test temperature of $750 \text{ }^{\circ}\text{C}$,

due to negligible $\alpha \rightarrow \beta$ phase transformation, contain higher fractions of α phase which amplifies α - α boundary interactions and hence void formation.

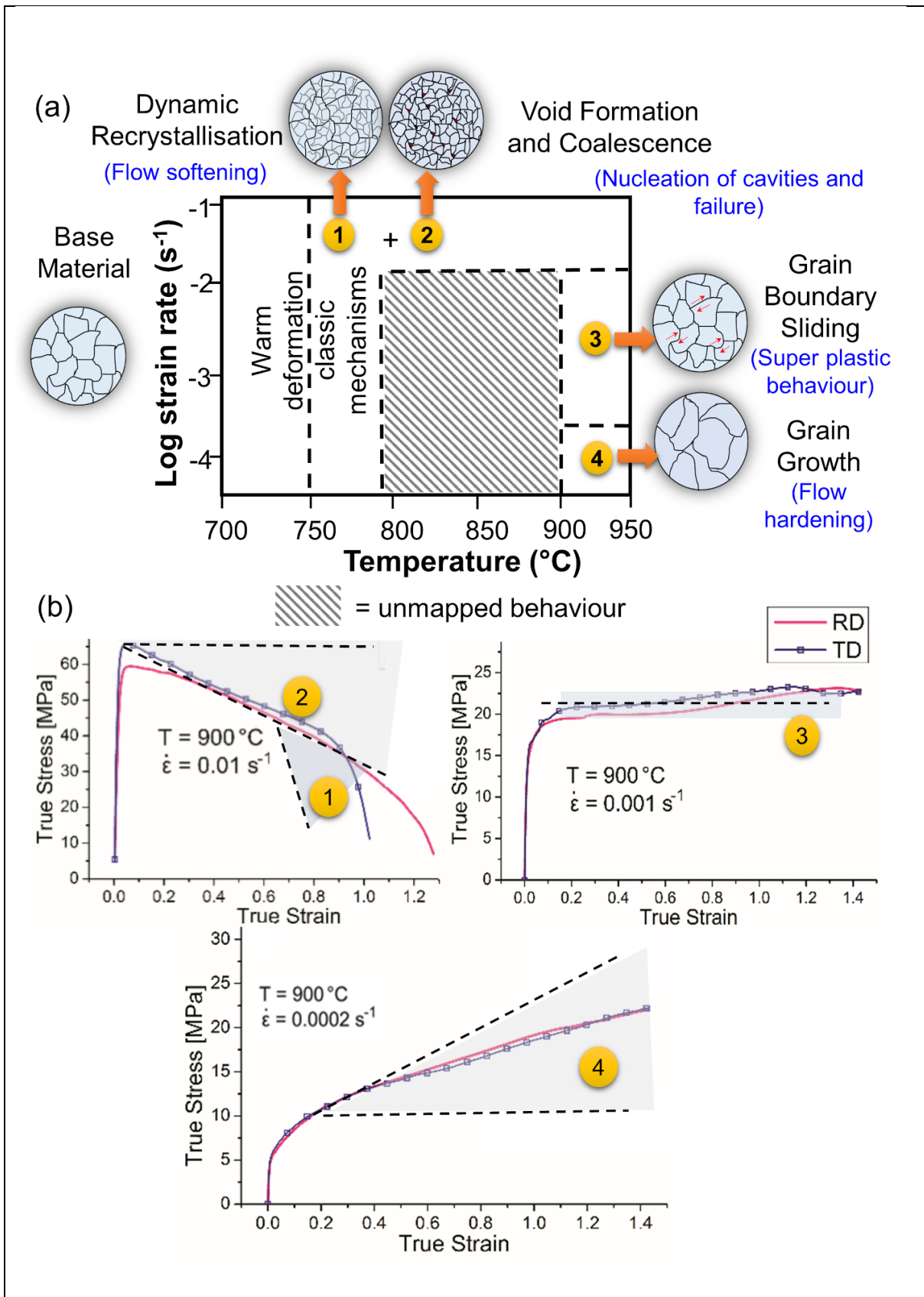
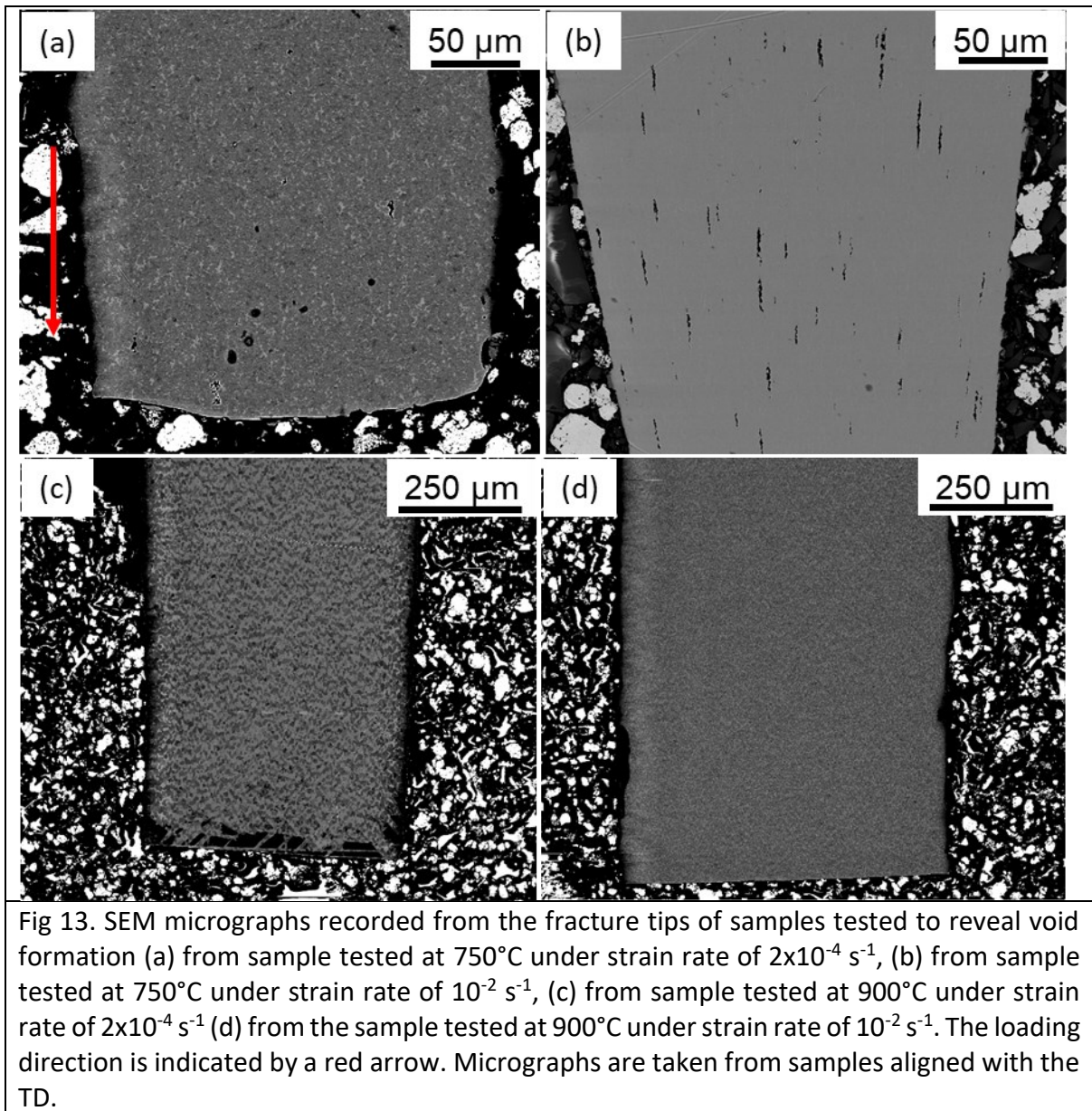


Fig 12.(a) A deformation plot for Ti-64 alloy identifying different deformation regimes based on temperature and strain rate (b) Schematic illustrations of the dominant deformation mechanisms expected to occur in each regime identified in (a).



High magnification SEM observations of the samples tested at 750 °C show that the micro cracks and voids appear to be predominantly associated with the α - α grain boundaries (Fig 14 (a, c)). For the tests conducted at 900 °C, owing to $\alpha \rightarrow \beta$ phase transformation, a higher fraction of β phase presents during the tests under slower stain rates where high levels of SPF were measured. For these conditions, the β phase appears to be arresting the propagation of the cracks initiated from within the α grains (Fig 14 (a)) as well as along α - α phase boundaries (Fig 14(e) and Fig 14(f)). This is thought to be due the higher ductility of the β phase at 900°C compared to those of the tests conducted at 750°C. This enables the β phase

to be ductile enough to blunt the cracks formed either within the α grains or along the α - α phase boundaries.

A previous report showed that if the overall deformation is governed by the α phase, the material is deformed in the iso-strain-rate mode, where the stress distribution between the α and β phases is such that the resultant matrix deformation rates in the two phases are equal [35]. Conversely, in the case of the iso-stress mode, the overall matrix deformation is rather controlled by the deformation of the β phase where the stress in the α and β phases are assumed to be equal resulting in a strain rate distribution between the two phases [36]. This is arguable for Ti-64 as Leader et al. [37] suggest that the iso-stress mode is more dominant, whereas Hamilton et. al [38] reported that the iso-strain-rate mode was dominant for superplastic forming behaviour. Though, the deformation mode appears to be dependent on the test temperature and strain rate.

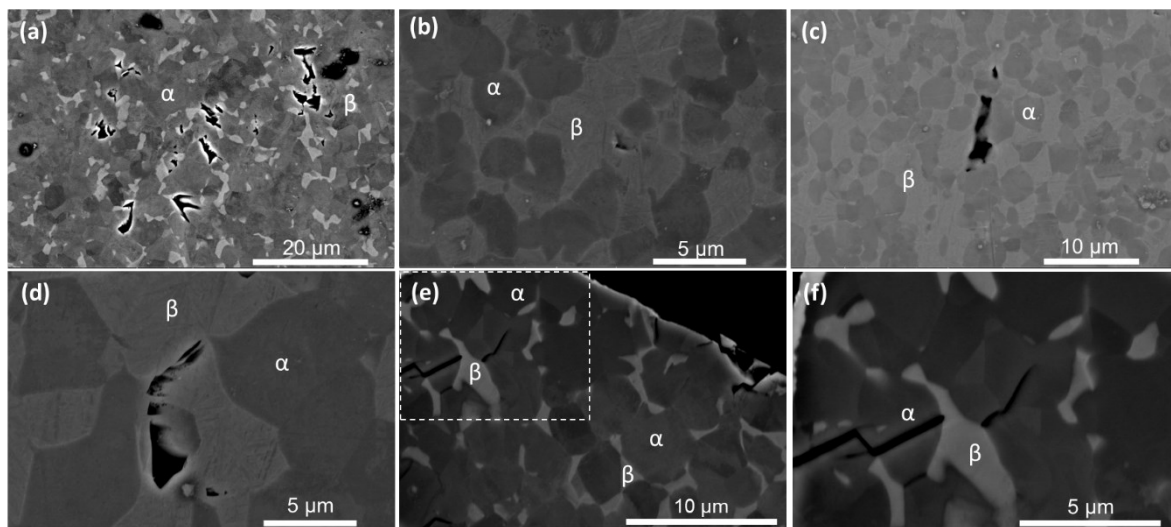


Fig 14. SEM micrographs showing the development of micro-voids/cracks during the test (a) at 750°C under $2 \times 10^{-4} \text{ s}^{-1}$ strain rate in a sample aligned with the TD, (b) and (c) at 750°C under 10^{-2} s^{-1} strain rate in samples aligned with the RD, (d) at 900°C under $2 \times 10^{-4} \text{ s}^{-1}$ strain rate in a sample aligned with the TD, and (e) and (f) at 900°C under 10^{-2} s^{-1} strain rate in a sample aligned with the TD.

In addition to the cavitation damage induced flow softening, the combined effects of dynamic recovery, dynamic recrystallisation, dynamic globularisation of α phase, and phase transformations occurring during deformation also contribute to the observed flow softening [8]. Jiang et. al [39] reported that dynamic softening of a hot deformed titanium alloy in the $\alpha + \beta$ regime was a result of dynamic recovery and dynamic recrystallisation processes where dynamic recrystallisation dominated below 800°C and dynamic recovery dominated above 800°C. It was found that both mechanisms were greatly influenced by the deformation conditions. The volume fraction of the α phase was found to decrease during deformation due to the increase in the stored energy, effectively promoting the $\alpha \rightarrow \beta$ phase transformation, also contributing to flow softening [40]. Lower temperatures were found to accelerate the phase transformation due to increased dislocation pile up. During deformation the lamellar α phase was seen to elongate, bend, fragment and spheroidise, something that is also observed in the study presented.

In general, globularisation of lamellar α phase can be classified into two main mechanisms, i.e., the boundary-splitting mechanism and termination migration mechanism [41]. The boundary-splitting mechanism can occur in both hot deformation and during heat treatment, while the termination migration mechanism usually takes place during heat treatment only [42]. So, it can be concluded that the transformation mechanisms of lamellar microstructures are attributed to the boundary-splitting mechanism in the present work. Lin et al. [41] also showed that the fraction of spheroidised α phase, and therefore high angle grain boundaries (HAGBs), was increased with increasing the test temperature which promotes the penetration of the β phase into the lamellar α phase, thus accelerating the fragmentation of lamellar α phase.

At the lower test temperature of 750 °C, under all strain rates, DRX is believed to occur, especially at low and moderate strains ($\epsilon < 0.5$). Previously reported physical based modelling of microstructure and mechanical property evolution has led to a reasonable convergence of previously predicted results towards the experimental data presented in this study [34]. However, the same approach based on the same assumptions did not respond well for higher levels of strain at this temperature.

The difference in fracture strain values observed under non-superplastic forming conditions have been investigated by many authors. Studies have related the anisotropy in plastic flow at elevated temperature to several influencing factors including (i) preferred orientation [22][32], (ii) active slip systems [23][24], (iii) banded microstructures [25][27], and (iv) grain size and morphology [43]. Later investigations suggest that these factors co-exist and it is difficult to isolate their individual effect [30][31].

For the test conducted at 900 °C and under slow to moderate strain rates ($\dot{\epsilon} < 0.001 \text{ s}^{-1}$), where the strain rate sensitivity value is larger than $m = 0.55$ (Fig 7), the deformation mechanism is dominated by grain boundary sliding (GBS) [44]. The measured stress-strain curve for this test displayed near steady-state flow stress (Fig 5(d)). This is an indication of a work hardening mechanism, such as grain growth or dislocation pile up, occurring fast enough to compensate for flow softening and DRX. Similarly, at 900°C and under the lowest strain rate, $2 \times 10^{-4} \text{ s}^{-1}$, strain hardening is observed. This implies that longer exposure time at this temperature results in dynamic grain coarsening and this is manifested in the increase in the measured average grain size for this test condition (Table 1) and also noticed clearly in EBSD results given in Fig 8 and Fig 9.

Studies on SPF behaviour of ultra-fine grain Ti-64 have claimed that the rate of dynamic coarsening is ≈ 10 to 20 times more rapid than that of static coarsening, owing to concurrent deformation and enhanced pipe diffusion associated with the generation of substructures in the β phase through which solutes are transported [36, 37]. Sargent et al. [46] have also demonstrated a quantitative link between the flow hardening and dynamic coarsening of equiaxed α grains during low-temperature superplastic deformation of an ultrafine grain Ti-64 billet when tested in compression mode. The test temperature of 900°C under slow strain rates resulted in a higher area fraction of β phase, which has been reported to provide very effective SPF properties [12], [13], [47]. However, steady state behaviour is also necessary to produce optimal superplastic forming [48], thus suggesting that 900°C and the intermediate strain rate of 10^{-2} s^{-1} is the optimum condition for superplasticity for this material. It was suggested that coarsening of α grains has a more pronounced effect on the mechanical properties due to an increase in the area fraction of β phase at 900°C in

combination with the slowest strain rate ($2 \times 10^{-4} \text{ s}^{-1}$). For these samples, a significantly smaller, if not free from, fraction of cavities was observed in the microstructure following SPF (Fig 13(e) and Fig 13(f)).

The measured anisotropic mechanical behaviours at 750 °C between the samples tested along the RD and the TD, in forms of differences in σ_{\max} and percentage of elongations, are likely to be due to the abundance of slip systems in the RD. This is because of the strong transverse texture and the presence of a weak basal component in the as-received material (Fig 2- Fig 4) which facilitate activation of more slip systems along the RD and therefore result in a slightly lower σ_{\max} and increased percentage of elongation (i.e., higher ductility) [5]. Also, the as-received microstructure (Fig 2) and those heated to the test temperatures (Fig 3 and Fig 4) show the presence of two types of micro-bands, one with equiaxed α grains aligned with the RD (Band AB), and the other with randomly distributed α and β grains with no preferred alignment (Band CD). These features have previously been observed to contribute to anisotropic deformation at elevated temperatures due to the higher resistance of α - α grain boundaries to GBS compared to α - β and β - β grain boundaries [25][26]. Moreover, sample cross-sections with a larger proportion of AB type banded microstructure were reported to have less superplasticity compared to those containing mainly the CD type bands. Ingelbrecht et al [49] has attributed the variation in deformation along the width and thickness during superplastic deformation of Ti-6Al-4V alloy to AB band type microstructure with α and β grains aligned with the RD.

The samples tested under 0.001 s^{-1} and 0.0002 s^{-1} strain rates at 900 °C displayed isotropic behaviour with no measurable difference in σ_{\max} along both the RD and the TD. This was under a condition where the initial material was strongly textured with a banded microstructure present (Fig 4). It is likely that under these testing conditions, GBS and grain growth (Fig 12) are the dominant mechanisms active during SPF. This is supported by the fact that only for samples exhibiting isotropic deformation behaviour does the percentage of elongation approach that of SPF, i.e., > 200% with higher m values ($m > 0.5$). Therefore, from all the test conditions, only two tests are exhibiting superplastic forming behaviour; those tested at the higher temperature of 900°C at intermediate and lower strain rates (i.e., 0.001 s^{-1} , 0.0002 s^{-1}).

There are two accommodation mechanisms that describe how boundary continuity is maintained during GBS. One of these mechanisms is termed Rachinger sliding [50] where GBS is accommodated by dislocations within the lattice, and the other is known as Lifshitz sliding [51] where stress driven diffusion compensates for the boundary. The former results in significant weakening or a complete disappearance of initial crystallographic texture [44]. In reality, it is possible for a range of accommodation mechanisms to happen concurrently, depending on the specific forming regime and material utilised [9], [44]. The values calculated for the stress exponent ' n ' (where $n = 1/m$ is the reciprocal ratio of the strain rate sensitivity ' m ' shown in Fig 7) of the material used in this study were ≈ 1.6 to 2.8. This suggests that GBS in this case was likely accommodated to various degrees by dislocation glide-climb which would yield $n = 2$ [52], [53] and diffusional processes for which $n = 1$ [45].

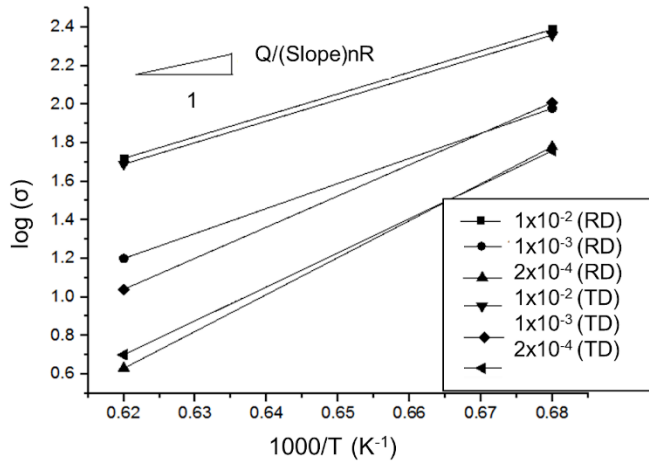


Fig 15. Plot of true stress as a function of temperature used for the calculation of activation energy (Q) at each temperature.

Table 3. Activation energies (Q) for different sample orientations at each temperature and strain rate applied in this work calculated using the slope of the stress- temperature plot in Fig 15.

Temperature, T	Strain rate, $\dot{\epsilon}$ (s ⁻¹)	Orientation	Activation Energy, Q (kJ/mol)
750°C	2x10 ⁻⁴	RD	442.72
		TD	419.74
	10 ⁻³	RD	300.23
		TD	384.12
	10 ⁻²	RD	257.96
		TD	265.34
900°C	2x10 ⁻⁴	RD	252.98
		TD	253.29
	10 ⁻³	RD	171.56
		TD	231.79
	10 ⁻²	RD	147.41
		TD	160.12

The activation energy for a specific deformation process also provides useful information on rate-controlling mechanisms. In this study, the activation energy, Q, was calculated from the flow stress data based on a method outlined by Ko et al. [54] in the form of Equation 3.

$$\dot{\epsilon} = A\sigma^n e^{(-Q/RT)} \quad (3)$$

Where A is the frequency factor, n is the stress exponent, R is the universal gas constant and T is the absolute temperature. Table 3 summarises the calculated Q for each test condition based on the plot of stress-temperature shown in Fig 15. The calculated Q for the tests carried out at 900 °C under 0.001s⁻¹ and 0.0002s⁻¹ strain rates, which exhibited SPF behaviour, ranges from 171.56 - 253.29 kJ/mol (Table 2). Previous reports suggested different Q values for

materials exhibiting SPF behaviour including $Q=216$ kJ/mol [55], 210 kJ/mol [56], $Q = 160$ kJ/mol [57] and $Q = 176$ kJ/mol [54]. The necessary Q for GBS was presented to be 174 kJ/mol for a material similar to this study [44] and therefore the calculated Q in Table 2 suggest that GBS is occurring during the tests conducted at 900 °C under slow strain rates. The calculated Q values in this study are also similar to that reported earlier by Arieli and Rosen [58] for grain-boundary diffusion in the superplastic regime of 800 °C to 950 °C for Ti-64 (*i.e.*, 189 kJ/ mol). Thus, it might be hypothesised that the deformation mechanism for the tests carried out at 900 °C is GBS accommodated by both grain-boundary diffusion and thermally activated dislocation glide-climb, *i.e.*, a combination of Ratchinger and Lifshitz sliding occurring concurrently.

In a recent study, Alabort et al. [44] investigated the superplastic formability of Ti-64 using in-situ micromechanical testing in conjunction with microscopic observations at temperatures in the range of 700 °C – 950 °C. The SEM results showed that optimum SPF behaviour was consistent with the dislocation based Ratchinger theory at higher forming temperatures (850 - 900 °C) and lower strain rates ($< 1 \times 10^{-3} \text{ s}^{-1}$). It was claimed that the volume fraction of the β phase is crucial in determining the deformation accommodation mechanism. At temperatures above 850°C it was determined that the majority of deformation occurs in the β grains while the α grains remain unaffected (*i.e.* undeformed), backed up by in-situ observation during deformation. However, at temperatures lower than 850°C the volume fraction of the β phase is reduced and intergranular slip bands were observed in α grains along with cavitation to facilitate GBS. There was reportedly a change from dislocation creep at high strain rates to GBS at lower strain rates, a transition reportedly due to a change in volume fraction of β phase [44]. This is primarily because the β phase is softer than the α phase with higher self-diffusivity coefficients and more available slip systems [1]. The increase in β phase also prevents excessive grain growth in the α phase which helps in maintaining a small α grain size that favours superplastic behaviour whilst promoting phase boundary sliding where α - β grain boundary sliding is preferred over α - α phase boundary sliding [35]. It was also reported that when the equilibrium sub-grain size (λ) is greater than the mean grain size (d) then Ratchinger GBS occurs under superplastic conditions. However, if λ is found to be smaller than d , then dislocation pile-up occurs that leads to the formation of sub-grain boundaries resulting in DRX [59]. This change in mechanism was supported by in-situ surface observations, experimental measurement of the strain rate sensitivity parameter, m , and analytical modelling [35]. This behaviour of DRX is thought to be typical of the close-to-superplastic high-strain-rate regime and the findings of Alabort et al [44] are in agreement with the results of this study. As in this study, flow softening and DRX are also observed for conditions close to SPF conditions at 750°C (Fig 5(e)). The similarity in findings is further corroborated by the calculated strain rate sensitivity values (Fig 7) that show an increase in strain rate sensitivity and thus the likelihood of GBS mechanisms getting activated at 900°C under low strain rates. It has been reported that 40-50% volume fraction of β is required to achieve the optimum SPF in the case of α - β titanium alloys [12], [13], [47].

The material tested at 750 °C under a lower strain rate of 0.0002 s⁻¹ shows a loss of texture with max MUDs of 1.98 and 1.89 for both ORD and 90RD sample orientations, respectively. The loss in texture intensity along with the measured flow softening behaviour (Fig 5) for this test condition is indicative of DRX, where the formation of new strain free grains of random orientation results in the loss of texture [60]. Samples subjected to the slower strain rates were exposed to the test temperature for longer times and therefore have more energy to undergo DRX compared to those tested under the higher strain rate of 0.01s⁻¹. This is in keeping with the previous findings of Alabort et al. [44] for the same alloy with a coarser starting grain size.

The texture results for the samples tested at 900 °C under the lower strain rate of 0.0002 s⁻¹ in the RD shows comparatively strong textures with max MUDs of 6.32 and 8.86 for the ND-TD and ND-RD planes, respectively, comparable to those tested under the same strain rate at 750 °C (Fig 10). This retention of texture and the flow hardening behaviour of the material (Fig 5) under these forming conditions suggests that DRX is not taking place completely. Instead, this suggests that most deformation has occurred in the β phase (i.e. iso-stress mode) and thus as the α grains are not deformed the activation energy for recrystallisation is much higher due to a lack of strain energy for nucleation of new α grains. The superplastic behaviour observed is facilitated by the increase in β phase at this temperature which is optimum for grain boundary sliding [12], [13], [47] and phase boundary sliding as α-β sliding is preferred over α-α sliding [35]. This lack of deformation in the α phase indicates that with increased exposure time, the dynamic grain coarsening phenomenon occurs at the higher temperature. As no significant change in texture is observed for the test at 900 °C under the strain rate of 0.0002 s⁻¹ in the RD which displayed superplastic forming behaviour, it is unlikely that the deformation is accommodated by Rachinger GBS as this is evidenced by a change in texture [10], [44].

The observed reduction in texture intensity during superplastic deformation may be attributed to GBS and the associated randomisation effect on the α grains. This is similar to the results reported previously for Ti-64 alloy [45]. This randomisation as a result of GBS however, is only observed in this study for the samples tested along the TD at 900°C and under 2×10⁻⁴ s⁻¹ strain rate (Fig 11). The samples tested along the RD under the same test conditions, which exhibited isotropic SPF behaviour, retained the texture with slightly weaker intensity. Therefore, although samples tested along both the RD and TD were undergoing GBS, it may be possible that the deformation in both orientations are accommodated by different dominant mechanisms, lifshitz or Rachinger sliding in either the iso-stress or iso strain rate mode.

5 Conclusions

In this study, evolution of mechanical properties, microstructure and crystallographic texture in a dual phase Ti-64 alloy have been investigated at superplastic forming regime (i.e.,

subjected to different strain rates at elevated temperatures). The main conclusions from the presented work are as follows:

- (1) Anisotropic tensile behaviour was observed for all tests at 750 °C disregarding the applied strain rate, whereas at 900 °C this was observed only under the relatively higher strain rate of 0.01s^{-1} . The observed anisotropy is shown to be due to the preferential slip system activations of the textured material during deformation under the conditions out with the superplastic forming regime where the dominant deformation mechanisms are slip driven and not grain boundary sliding.
- (2) At high temperatures and under moderate strain rates, 900 °C and $\dot{\epsilon} < 0.001\text{ s}^{-1}$, isotropic superplastic forming behaviour was observed in the textured material where the conditions were satisfying the superplastic forming regime and grain boundary sliding was justified to be the major deformation mechanism.
- (3) The ductile damage induced flow stress softening behaviour of tests exhibiting anisotropic behaviour is thought to be the result of nucleation and growth of micro-voids and their coalescence into macro-cracks. The compatibility requirements at the interface between α - α , α - β and along pre-existing β grain boundaries is thought to be the main driving force for nucleation of voids during hot tensile deformation.
- (4) It is likely that a combination of Rachinger grain boundary sliding and Lifshitz sliding is occurring to accommodate grain boundary sliding at 900 °C under the slower strain rates, $< 0.001\text{ s}^{-1}$, where one may dominate the deformation depending on texture and the sample orientation.

The raw/processed data required to reproduce these findings cannot be shared at this time as the data also forms part of an ongoing study.

6 References

- [1] J. Sieniawski, M. Motyka "Superplasticity in titanium alloys Superplasticity in titanium alloys," *J. Achiev. Mater. Manuf. Eng.*, vol. 24, no. 1, pp. 123-130, 2007.
- [2] G. Lütjering, "Influence of processing on microstructure and mechanical properties of (α + β) titanium alloys," *Mater. Sci. Eng. A*, vol. 243, no. 1–2, pp. 32–45, 1998.
- [3] R. R. Boyer, "An overview on the use of titanium in the aerospace industry," vol. 213, pp. 103–114, 1996.
- [4] B. M. Li, J. F. Han, G. M. Xu, and J. Z. Cui, "Effect of cold-rolling and annealing on interfacial structures and properties of A500/steel bimetal strip," *Trans. nonferrous Met. Soc. China*, vol. 15, no. 4, pp. 754–758, 2005.
- [5] K. Sofinowski, M. Šmíd, S. van Petegem, S. Rahimi, T. Connolley, and H. van Swygenhoven, "In situ characterization of work hardening and springback in grade 2 α -titanium under tensile load," *Acta Mater.*, vol. 181, pp. 87–98, 2019, doi: 10.1016/j.actamat.2019.09.039.
- [6] S. Khayatzadeh, M. J. Thomas, Y. Millet, and S. Rahimi, "Characterisation and modelling of in-plane springback in a commercially pure titanium (CP-Ti)," *J. Mater. Sci.*, vol. 53, no. 9, pp. 6872–6892, 2018, doi: 10.1007/s10853-017-1983-8.
- [7] S. Khayatzadeh, S. Rahimi, and P. Blackwell, "Effect of plastic deformation on elastic and plastic recovery in CP titanium," *Key Eng. Mater.*, vol. 716, no. July, pp. 891–896,

- 2016, doi: 10.4028/www.scientific.net/KEM.716.891.
- [8] H. Yang, X. Fan, Z. Sun, L. Guo, and M. Zhan, "Recent developments in plastic forming technology of titanium alloys," *Sci. China Technol. Sci.*, vol. 54, no. 2, pp. 490–501, 2011.
 - [9] G. E. Dieter, *Mechanical Metallurgy*, SI Metric. Singapore: McGraw-Hill Book Co., 1988.
 - [10] T. G. Langdon, "Seventy-five years of superplasticity : historic developments and new opportunities," pp. 5998–6010, 2009, doi: 10.1007/s10853-009-3780-5.
 - [11] D. H. Buckley, "The Influence of the Atomic Nature of Crystalline Materials on Friction," *A S L E Trans.*, vol. 11, no. 2, pp. 89–100, 1968, doi: 10.1080/05698196808972212.
 - [12] N. Ridley, *Metals for superplastic forming*. Woodhead Publishing Limited.
 - [13] T.-G. Nieh, J. Wadsworth, and O. D. Sherby, *Superplasticity in metals and ceramics*. Cambridge university press, 2005.
 - [14] R. March, "The Rate Controlling Mechanism in Superplasticity," 1971.
 - [15] S. Hori, M. Tokzane, and N. Furushiro, "Superplasticity in Advanced Materials (ICSAM-91)," *Osaka JSRS*, 1991.
 - [16] A. H. Chokshi, A. K. Mukherjee, and T. G. Langdon, "Superplasticity in advanced materials," *Mater. Sci. Eng. R Reports*, vol. 10, no. 6, pp. 237–274, 1993.
 - [17] M. O. J.H.W. de Wit, A. Demaid, "Case Studies in manufacturing with advanced materials," in *Case Studies in manufacturing with advanced materials*, 1st ed., Amsterdam, 1992, pp. 35–71.
 - [18] "Superplastic forming (SPF) of materials and SPF combined with diffusion bonding Technological and design aspects.pdf." .
 - [19] A. J. Barnes, "Superplastic Forming 40 Years and Still Growing," vol. 16, no. August, pp. 440–454, 2007, doi: 10.1007/s11665-007-9076-5.
 - [20] L. Papeleux and J. Ponthot, "Finite element simulation of springback in sheet metal forming," vol. 126, pp. 785–791, 2002.
 - [21] O. A. Kaibyshev, "Fundamental aspects of superplastic deformation," vol. 324, no. 0921, pp. 96–102, 2002.
 - [22] A. D. Sheikh-Ali and H. Garmestani, "On the independent behavior of grain boundary sliding and intragranular slip during superplasticity," in *Materials science forum*, 2001, vol. 357, pp. 393–398.
 - [23] C. M. Packer, R. H. Johnson, and O. D. Sherby, "Evidence for the Importance of Crystallographic Slip During Superplastic Deformation of Eutectic," vol. 242, no. December, pp. 2485–2489, 1988.
 - [24] H. Naziri and R. Pearce, "The influence of copper additions on the superplastic forming behaviour of the Zn? Al eutectoid," *Int. J. Mech. Sci.*, vol. 12, no. 6, pp. 513–521, 1970.
 - [25] D. S. McDermid, A. W. Bowen, and P. G. Partridge, "Superplastic deformation of strongly textured Ti-6Al-4V - Part 2 changes in microstructure and texture," *J. Mater. Sci.*, vol. 20, no. 6, pp. 1976–1984, 1985, doi: 10.1007/BF01112279.
 - [26] P. G. Partridge, D. S. McDermid, and A. W. Bowen, "A deformation model for anisotropic superplasticity in two phase alloys," *Acta Metall.*, vol. 33, no. 4, pp. 571–577, 1985.
 - [27] A. W. Bowen, D. S. McDermid, and P. G. Partridge, "Effect of high-temperature deformation on the texture of a two-phase titanium alloy," *J. Mater. Sci.*, vol. 26, no. 13, pp. 3457–3462, 1991, doi: 10.1007/BF00557131.
 - [28] O. Benay, A. S. Lucas, A. Vadon, and S. Obadia, "Relations between Texture, Superplastic Deformation and Mechanical Properties of Thin TA6V Slabs," in *Materials*

- Science Forum*, 1994, vol. 157, pp. 1357–1364.
- [29] Y. Wang, W. He, N. Liu, A. Chapuis, B. Luan, and Q. Liu, "Effect of pre-annealing deformation on the recrystallized texture and grain boundary misorientation in commercial pure titanium," *Mater. Charact.*, vol. 136, pp. 1–11, 2018.
- [30] G. L. Dunlop, J. D. Reid, and D. M. R. Taplin, "Anisotropic ductility of a superplastic aluminum bronze," *Metall. Mater. Trans. B*, vol. 2, no. 8, pp. 2308–2310, 1971, doi: 10.1007/BF02917577.
- [31] D. Lee and E. W. Hart, "Stress relaxation and mechanical behavior of metals," *Metall. Trans.*, vol. 2, no. 4, pp. 1245–1248, 1971, doi: 10.1007/BF02664258.
- [32] V. V. Astanin, O. A. Kaibyshev, and S. N. Faizova, "Cooperative grain boundary sliding under superplastic flow," *Scr. Metall. Mater.*, vol. 25, no. 12, pp. 2663–2668, 1991.
- [33] ASTM International, *ASTM E2448-18, Standard Test Method for Determining the Superplastic Properties of Metallic Sheet Materials*. West Conshohocken, PA, 2018.
- [34] E. Alabort, D. Putman, and R. C. Reed, "Superplasticity in Ti-6Al-4V: Characterisation, modelling and applications," *Acta Mater.*, vol. 95, pp. 428–442, 2015, doi: 10.1016/j.actamat.2015.04.056.
- [35] J. S. Kim, J. H. Kim, Y. T. Lee, C. G. Park, and C. S. Lee, "Microstructural analysis on boundary sliding and its accommodation mode during superplastic deformation of Ti – 6Al – 4V alloy," vol. 263, pp. 272–280, 1999.
- [36] C. S. Lee, S. B. Lee, J. S. Kim, and Y. W. Chang, "Mechanical and microstructural analysis on the superplastic deformation behavior of Ti } 6Al } 4V Alloy," vol. 42, 2000.
- [37] J. R. Leader, D. F. Neal, and C. Hammond, "The effect of alloying additions on the superplastic properties of Ti-6 pct Al-4 pct V," *Metall. Trans. A*, vol. 17, no. 1, pp. 93–106, 1986.
- [38] D. F. Hasson and C. H. Hamilton, "Advanced processing methods for titanium," 1982.
- [39] Y. Q. Jiang, Y. C. Lin, X. Y. Jiang, D. G. He, X. Y. Zhang, and N. Kotkunde, "Hot tensile properties, microstructure evolution and fracture mechanisms of Ti-6Al-4V alloy with initial coarse equiaxed phases," *Mater. Charact.*, vol. 163, no. October 2019, p. 110272, 2020, doi: 10.1016/j.matchar.2020.110272.
- [40] I. Balasundar, K. R. Ravi, and T. Raghu, "On the high temperature deformation behaviour of titanium alloy BT3-1," *Mater. Sci. Eng. A*, vol. 684, pp. 135–145, 2017.
- [41] Y. C. Lin, Q. Wu, G. D. Pang, X. Y. Jiang, and D. G. He, "Hot Tensile Deformation Mechanism and Dynamic Softening Behavior of Ti-6Al-4V Alloy with Thick Lamellar Microstructures," *Adv. Eng. Mater.*, vol. 22, no. 3, pp. 1–11, 2020, doi: 10.1002/adem.201901193.
- [42] Y. Q. Ning, X. Luo, H. Q. Liang, H. Z. Guo, J. L. Zhang, and K. Tan, "Competition between dynamic recovery and recrystallization during hot deformation for TC18 titanium alloy," *Mater. Sci. Eng. A*, vol. 635, pp. 77–85, 2015, doi: 10.1016/j.msea.2015.03.071.
- [43] Y. B. Xu *et al.*, "Shear localization and recrystallization in dynamic deformation of 8090 Al-Li alloy," *Mater. Sci. Eng. A*, vol. 299, no. 1–2, pp. 287–295, 2001, doi: 10.1016/S0921-5093(00)01412-X.
- [44] E. Alabort, P. Kontis, D. Barba, K. Dragnevski, and R. C. Reed, "Acta Materialia On the mechanisms of superplasticity in Ti e 6Al e 4V," *Acta Mater.*, vol. 105, pp. 449–463, 2016, doi: 10.1016/j.actamat.2015.12.003.
- [45] S. L. Semiatin *et al.*, "Plastic Flow and Microstructure Evolution during Low-Temperature Superplasticity of Ultrafine Ti-6Al-4V Sheet Material," vol. 41, no. February, pp. 499–512, 2010, doi: 10.1007/s11661-009-0131-8.

- [46] G. A. Sargent, A. P. Zane, P. N. Fagin, A. K. Ghosh, and S. L. Semiatin, "Low-temperature coarsening and plastic flow behavior of an alpha/beta titanium billet material with an ultrafine microstructure," *Metall. Mater. Trans. A*, vol. 39, no. 12, p. 2949, 2008.
- [47] G. A. Salishchev, E. A. Kudrjavitsev, S. V. Zhrebtsov, and S. L. Semiatin, "Low Temperature Superplasticity of Ti-6Al-4V Processed by Warm Multidirectional Forging," vol. 735, pp. 253–258, 2013, doi: 10.4028/www.scientific.net/MSF.735.253.
- [48] E. Alabort, D. Putman, and R. C. Reed, "Acta Materialia Superplasticity in Ti – 6Al – 4V : Characterisation , modelling and applications," vol. 95, pp. 428–442, 2015, doi: 10.1016/j.actamat.2015.04.056.
- [49] C. D. Ingelbrecht and P. G. Partridge, "Superplastic deformation of sheet test pieces machined from Ti-6Al-4V bar," *J. Mater. Sci.*, vol. 21, no. 11, pp. 4071–4080, 1986, doi: 10.1007/bf00553471.
- [50] T. G. Langdon, "A unified approach to grain boundary sliding in creep and superplasticity," *Acta Metall. Mater.*, vol. 42, no. 7, pp. 2437–2443, 1994.
- [51] W. R. Cannon and W. D. Nix, "Models for grain rearrangement resulting from grain boundary sliding," *Philos. Mag.*, vol. 27, no. 1, pp. 9–16, 1973.
- [52] R. Gifkins, "Grain-boundary sliding and its accommodation during creep and superplasticity," *Metall. Trans. a*, vol. 7, no. 8, pp. 1225–1232, 1976.
- [53] M. Kawasaki and T. G. Langdon, "Principles of superplasticity in ultrafine-grained materials," *J. Mater. Sci.*, vol. 42, no. 5, pp. 1782–1796, 2007.
- [54] Y. G. Ko, C. S. Lee, D. H. Shin, and S. L. Semiatin, "Low-Temperature Superplasticity of Ultra-Fine-Grained Ti-6Al-4V Processed by Equal-Channel Angular Pressing," vol. 37, no. FEBRUARY, pp. 381–391, 2006.
- [55] M. L. Meier, D. R. Lesuer, and A. K. Mukherjee, " α Grain size and β volume fraction aspects of the superplasticity of Ti-6Al-4V," *Mater. Sci. Eng. A*, vol. 136, pp. 71–78, 1991.
- [56] T. Seshacharyulu, S. C. Medeiros, W. G. Frazier, and Y. Prasad, "Hot working of commercial Ti-6Al-4V with an equiaxed α - β microstructure: materials modeling considerations," *Mater. Sci. Eng. A*, vol. 284, no. 1–2, pp. 184–194, 2000.
- [57] S. L. Semiatin and G. A. Sargent, "Constitutive modeling of low-temperature superplastic flow of ultrafine Ti-6Al-4V sheet material," in *Key Engineering Materials*, 2010, vol. 433, pp. 235–240.
- [58] A. Arieli and A. Rosen, "Superplastic deformation of Ti-6Al-4V alloy," *Metall. Trans. A*, vol. 8, no. 10, pp. 1591–1596, 1977.
- [59] T. G. Langdon, "Grain boundary sliding revisited : Developments in sliding over four decades," vol. 1, pp. 597–609, 2006, doi: 10.1007/s10853-006-6476-0.
- [60] A. Rollett, F. J. Humphreys, G. S. Rohrer, and M. Hatherly, *Recrystallization and related annealing phenomena*. Elsevier, 2004.